

The optimum fire window: applying the fire-productivity hypothesis to Jurassic climate states

Teuntje P. Hollaar*^{1,2}, Claire M. Belcher¹, Micha Ruhl³, Jean-François Deconinck⁴, Stephen P. Hesselbo^{2,5}

¹WildFIRE Lab, Global Systems Institute, University of Exeter, Exeter, EX4 4PS, UK

²Camborne School of Mines, Department of Earth and Environmental Sciences, University of Exeter, Penryn Campus, Penryn, TR10 9FE, UK

³Department of Geology, Trinity College Dublin, The University of Dublin, College Green, Dublin, Ireland

⁴Biogéosciences, UMR 6282 CNRS, Université de Bourgogne/Franche-Comté, 21000 Dijon, France

⁵Environment and Sustainability Institute, University of Exeter, Penryn Campus, Penryn, TR10 9FE, UK

*Corresponding author: t.p.hollaar@uu.nl

Abstract

Present day fire frequency has been related to a productivity/aridity gradient on a regional and global scale. Optimum fire conditions occur at times of intermediate productivity and aridity, whereas fire is limited on the high productivity (moisture) and aridity (no fuel) endmembers. However, the current global fire activity pattern is reinforced by the predominant burning of grasslands. Here we test the intermediate fire-productivity hypothesis for a period on Earth before the evolution of grasses, the Early Jurassic, and explore the fire regime of two contrasting climatic states: the Late Pliensbachian (LPE) cooling Event and the Sinemurian–Pliensbachian Boundary (SPB) warming. Palaeo-fire records are reconstructed from fossil charcoal abundance, and changes in the hydrological cycle are tracked via clay mineralogy, which allows inference of changes in fuel moisture status. Large fluctuations in the fossil charcoal on an eccentricity time scale indicate two modes of fire regime at the time. Wildfires were moisture limited in a high productivity ecosystem during eccentricity minima for both the SPB and LPE. During eccentricity maxima, fires increased, and an optimum fire window was reached, in which greater seasonality in rainfall and temperatures led to intermediate states of productivity and aridity. The LPE experienced more extreme climatic endmembers compared to the SPB, with the fire regime edging closer to ‘moisture limitation’ during eccentricity minima, and more

34 pronounced seasonality during eccentricity maxima, explained by the overall cooler climate at the
35 time. This study illustrates that the intermediate-productivity gradient holds up during two contrasting
36 climatic states in the Jurassic.

37

38 **Plain Language Summary**

39 Fires are limited in year-round wet climates (tropical rainforests, too wet), and in year-round dry
40 climates (deserts, no fuel). This concept, the intermediate-productivity gradient, explains the global
41 pattern of fire activity. Here we test this concept for climate states of the Jurassic (~190 Myr ago). We
42 find that the intermediate-productivity gradient also applies in the Jurassic, despite the very different
43 ecosystem assemblages, with fires most frequent at times of high seasonality.

44

45 **Key Points**

- 46 • The intermediate-fire productivity gradient can be applied to the Jurassic and be utilized to
47 explain changes in biomass abundance, moisture availability, and fire activity.
- 48 • The terrestrial ecosystem surrounding the Cardigan Bay Basin was not year-round dry during
49 the Sinemurian–Pliensbachian Boundary warming Event or the Late Pliensbachian Cooling
50 Event and therefore fire was not aridity limited.
- 51 • Fire activity was strongly influenced by the ~100 kyr and 405 kyr eccentricity cycle during
52 both climatic states, which led to two modes in the fire regime: productivity limited (minima)
53 and the optimum fire-window (maxima).

54

55

56

57

58

59

60

61

62

63 **1 Introduction**

64 The global distribution of fire at the present day follows the intermediate-productivity hypothesis.
65 This hypothesis suggests that fire activity increases non-linearly along a productivity gradient
66 primarily controlled by biomass and fuel availability (Pausas & Bradstock, 2007; Pausas & Ribeiro,
67 2013). Climate drives fuel availability, structure, and moisture, which are the main determinants of the
68 fire regime. Where the fire regime reflects the frequency, behaviour, type of fire, and the impact on
69 the ecosystem (Bradstock, 2010). Fire is either limited by high moisture in ecosystems with high
70 biomass production, for example in tropical rainforests, or in high aridity and low biomass production
71 ecosystems, with disconnected fuel such as in deserts. This principle explains drought-driven fire
72 regimes and fuel-limited fire regimes (Pausas & Ribeiro, 2013). In humid regions fires are initiated by
73 seasonal aridity which leads to flammable conditions and lower fuel-moisture status. Rising
74 temperatures can lead to increased drought and flammability in high productivity ecosystems and
75 further accelerate this drought-driven increase in fire activity (Pausas & Ribeiro, 2013). In
76 unproductive arid regions it is biomass production that determines fire activity, as the fuel-moisture
77 status would not be limiting (Pausas & Ribeiro, 2013). The optimum window for wildfires is at
78 intermediate productivity levels, such as in the tropical savannahs of today, wherein biomass can
79 accumulate due to seasonal precipitation and fuel becomes available in the dry season when the fuel
80 moisture status decreases (Meyn et al., 2007; Pausas & Bradstock, 2007; Krawchuk & Moritz, 2011;
81 Pausas & Paula, 2012; Pausas & Ribeiro, 2013).

82

83 The intermediate-productivity concept provides an effective explanation for the distribution of fire on
84 a global and regional scale in the modern day where highest fire activity is found at intermediate
85 moisture availability (Meyn et al., 2007; Krawchuk & Moritz, 2011; Daniau et al., 2012). The
86 observation of high fire activity in ecosystems that are of intermediate aridity and productivity is
87 strongly driven by grass biomes today (Archibald et al., 2018), where >80 % of area burnt is in
88 grasslands (van der Werf et al., 2006). Although the intermediate-productivity gradient hypothesis of
89 the present day is strongly linked to the expanse of grassland habitats, it should not require the
90 presence of grasses to explain the impact of climate and seasonality on fire frequency in other
91 vegetation types. The crucial concept is that an optimum fire window exists when there is a
92 sufficiently moist season that allows fuel growth which is followed by a drier season in which fuel
93 moisture levels are lowered, allowing ignition and fire spread. Since fire has formed an important part
94 of ecosystems and the Earth system since 420 Ma (Glasspool et al., 2004; Glasspool & Gastaldo,
95 2022), we therefore test whether the intermediate-productivity gradient has also existed and if the
96 concept can also be applied in a world before the evolution of grasses.

97

98 Here we look back at two contrasting climate events in the Early Jurassic, ~190 Myr ago, to assess
99 what evidence there is for the existence of the intermediate-productivity fire gradient at such time

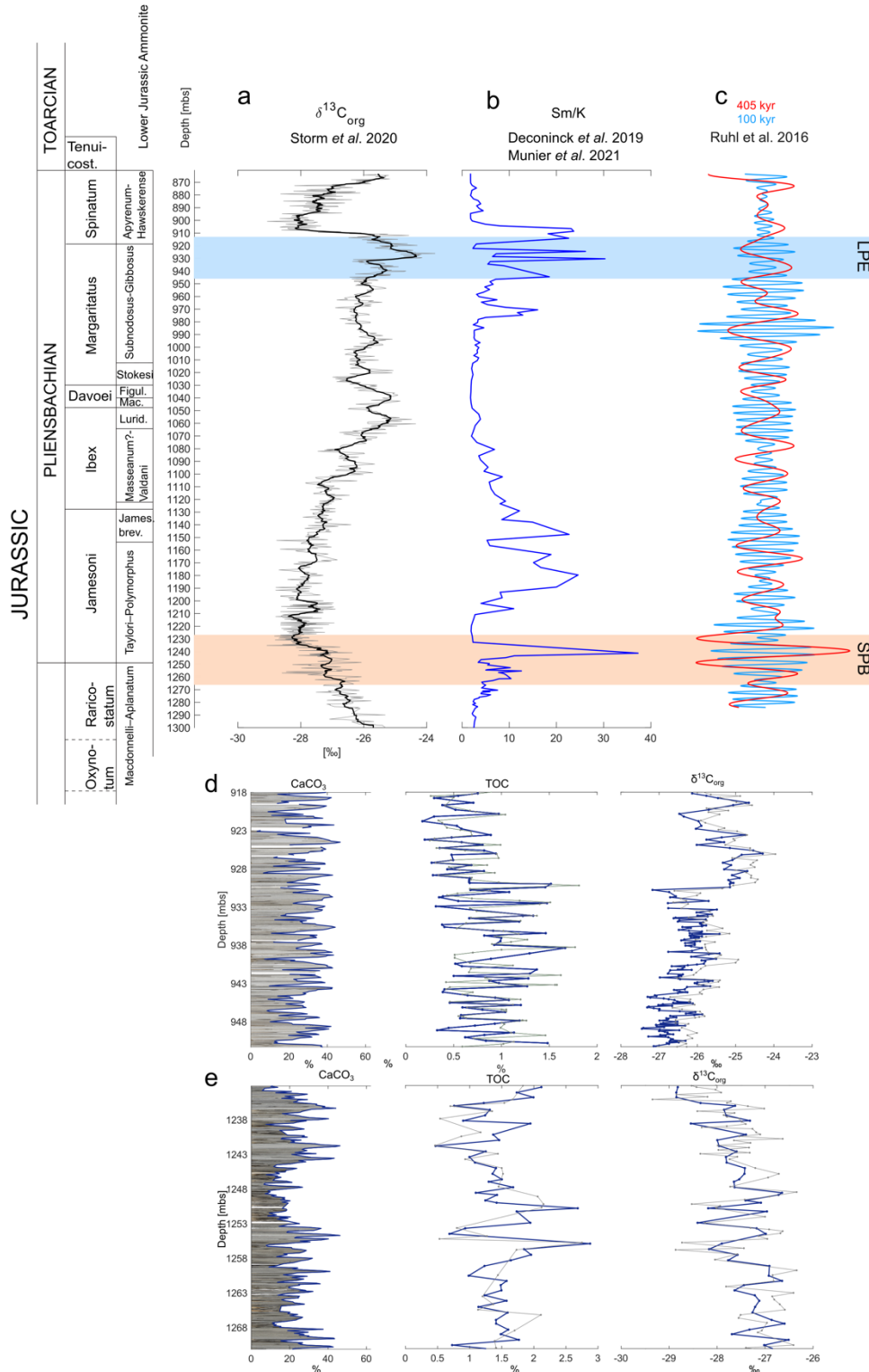
100 (Fig. 1). The first event, the Sinemurian-Pliensbachian Boundary event (SPB, is marked by global
101 warming, sea-level rise, increased humidity, and a negative carbon-isotope excursion (Ruhl et al.,
102 2016; Haq, 2018; Deconinck et al., 2019; Storm et al., 2020). In contrast, the second event, the late
103 Pliensbachian Event (LPE) is marked by ~ 5 °C cooling in NW Europe, greater aridity, sea-level fall
104 and a global positive carbon-isotope excursion (e.g. Korte et al., 2015; Ruhl et al., 2016; Haq, 2018;
105 Deconinck et al., 2019; Storm et al., 2020). We couple charcoal, clay and climate data to infer palaeo-
106 fire and the hydrological regimes during both these time intervals.

107

108 2 Materials and Methods

109 Materials

110 The records from both the LPE and SPB are taken from the Llanbedr (Mochras Farm) borehole, from
111 sedimentary strata deposited in a relatively deep marine setting close to the shore in the Cardigan Bay
112 Basin (Wales, UK). These sediments show a strong regular orbital control in the limestone-mudstone
113 alternations (Ruhl et al., 2016), and an existing astrochronological framework provides an age model
114 for the Mochras borehole. In addition, input of terrestrial organic matter in the sampled section is
115 relatively high (van de Schootbrugge et al., 2005; Riding et al., 2013), and thus provides ideal
116 material to study palaeo-fire regimes with a relatively high temporal constraint.



117

118 **Fig. 1:** Cyclostratigraphic framework of the latest Sinemurian–Pliensbachian of the Mochras core
 119 and the two intervals here studied. Red bar represents the interval (1271–1233 metres below surface
 120 (mbs)) of the SPB and the blue bar represents the interval of the LPE (951–918 mbs) (a) The $\delta^{13}\text{C}_{\text{org}}$
 121 record from the Mochras core (Storm et al., 2020), shows the broad negative carbon-isotope trend
 122 around the SPB and the positive carbon-isotope excursion (CIE) in the Late Pliensbachian. (b) The

123 *smectite/kaolinite (Sm/K) ratio reflects changes in the hydrological cycle; data from Deconinck et al.*
124 *(2019) and Munier et al. (2021). Peaks in smectite indicate greater climatic aridity (Deconinck et al.,*
125 *2019; Munier et al., 2021). (c) The bandpass-filtered Ca-elemental record in the depth domain from*
126 *Ruhl et al. (2016) representing the 100 kyr and 405 kyr cycle. (d) The LPE interval is carbonate-rich*
127 *and shows the metre-scale variations in CaCO₃ and TOC, next to the $\delta^{13}C_{org}$ positive shifts that marks*
128 *the onset of the LPE. (e) The SPB interval contains relatively more clay and lithological couplets of*
129 *alternating CaCO₃ and TOC-enhanced beds occurring on a metre scale. The $\delta^{13}C_{org}$ shows the*
130 *negative trend of the long-negative limb of the SPB negative CIE.*

131 The Mochras core was drilled between 1967 and 1969 on the coast in NW Wales, UK. Preserved 1-m-
132 length core slabs of the core are stored at the British Geological Survey National Core Repository at
133 Keyworth, United Kingdom. The Pliensbachian of Mochras shows alternating beds of pale grey
134 limestone and dark brown to grey mudstone (Ruhl et al., 2016). These couplets occur throughout the
135 Pliensbachian, but vary in thickness, from about 90 cm at the Sinemurian–Pliensbachian boundary to
136 about 30 cm in the Late Pliensbachian age strata (latest Margaritatus and Spinatum zones) (Ruhl et al.,
137 2016). The lithological couplets are well expressed around the SPB and in the Margaritatus Zone
138 (Ruhl et al., 2016). For this study, samples were taken at an average sample spacing of 90 cm across
139 the Sinemurian–Pliensbachian boundary (1272–1233 mbs (metres below surface)). In addition, data
140 are utilized in this study that are published in Hollaar et al. (2021; 2023), from the Late Pliensbachian
141 interval that is sampled at a 10 cm (951–934 mbs) and 30 cm (934–918 mbs) resolutions. The
142 macrocharcoal data between 934–918 mbs are new and not previously published. An overview of the
143 number of samples per stratigraphic interval and proxy can be found in SI Table 1.

144 *Palaeolocation and provenance*

145 During the Early Jurassic, the Mochras site was situated in the Boreal realm of the Laurasian Seaway,
146 which contained an island archipelago, and covers most of present-day NW and W Europe. The
147 Mochras site was situated at a palaeolatitude of $\sim 35^\circ$ N (Torsvik & Cocks, 2017), just off the Welsh
148 Massif, in a relatively deep marine setting, below storm base (Pieńkowski et al., 2021), but with a
149 strong terrestrial influence (van de Schootbrugge et al., 2005; Riding et al., 2013; Xu et al., 2018;
150 Storm et al., 2020).

151 The Welsh Massif was likely the main detrital source to the Cardigan Bay Basin (Deconinck et al.,
152 2019), although other emergent areas in proximity likely also contributed (Deconinck et al., 2019).
153 The nearby Irish Massif, situated west of the Welsh Massif, also cannot be dismissed as a source of
154 nutrients, terrestrial organic particles, clay and coarser mineral grains to the Cardigan Bay Basin
155 (Deconinck et al., 2019). Another possible source area is the emergent land of the Scottish Massif to
156 the north of the Mochras Borehole and the London-Brabant Massif to the east of the Mochras
157 Borehole (van de Schootbrugge et al., 2005).

158 The multiple nearby landmasses contributing runoff to the here studied relatively deeper marine
159 depositional environment, allowed for the charcoal record presented in this study to reflect a regional
160 expression of likely multiple fires. These fires might have in part occurred synchronous, but it is also
161 important to note that one stratigraphic rock sample in this study represents a ~2 kyr average signal,
162 which likely is more than the fire return interval at the time of deposition and thus represents an
163 averaging of the overall fire signal through time and space. Therefore, the term ‘fire activity’ here
164 describes the overall occurrences as increases and decreases in wildfires across the region.

165 In this study we measure the abundance of microcharcoal and macrocharcoal as a proxy for fire
166 activity. The size of charcoal fragments is often used as an indicator if the fires were proximal or
167 distal to the deposition site. Often larger more proximal charcoal particles are found in terrestrial
168 biomes and their depositional environments, in soils, lakes and mires. In contrast, smaller charcoal
169 particles that are wind-blown could potentially end up in a marine environment, as well as in more
170 distal terrestrial settings. However, experimental research showed that riverine transport has the
171 potential to carry the larger charcoal particles further away from shore, with the smaller charcoal
172 particles becoming water saturated at a shorter distance and settling down closer to the shoreline
173 (Nichols et al., 2000). In addition to this, other studies have indicated that larger charcoal particles (up
174 to 7 cm) can be windblown and travel up to 50 km from the original source, depending mainly on
175 their morphology (Woodward & Haines, 2020). Combined, charcoal size, shape, properties, wind
176 direction, plume height, but also riverine and marine transportation, all have a different impact on the
177 travel distance of different charcoal size classes. Hence, in the context of this study, no inferences can
178 be made about the different size classes and therefore microcharcoal and macrocharcoal both serve as
179 an overall indicator of fire activity.

180

181 *Methods*

182 Mass spectrometry $\delta^{13}\text{C}_{\text{org}}$, TOC and CaCO_3

183 Bulk organic carbon-isotopes, TOC and carbonate content were measured to track changes in the
184 carbon-cycle and changes in total organic matter in the studied interval. For the SPB interval (1271–
185 1233 mbs) 50 samples and for the LPE (918–951 mbs) 193 samples were processed for carbon
186 isotope mass spectrometry. Bulk rock samples were powdered using a pestle-a-mortar, weighed into
187 centrifuge tubes, and decarbonated using 3.3 % HCl. Following, the samples were transferred to a hot
188 bath (79 °C) for 1 h to remove siderite and dolomite. After this, the samples were centrifuged and the
189 liquid decanted, this step repeated until the samples were neutralized (on average 2 times). Finally, the
190 samples were oven-dried, re-powdered, and weighed (to measure CaCO_3 loss) and transferred into
191 small tin capsules for mass spectrometry (TOC and $\delta^{13}\text{C}_{\text{org}}$), at the University of Exeter, Penryn
192 Campus.

193 Charcoal quantification and palynofacies

194 For the SPB interval, 54 samples were prepared for charcoal analysis and 42 for palynofacies at the
195 University of Exeter, Streatham Campus. For the LPE interval, an additional 50 macrocharcoal
196 samples were analysed, to compliment a total of 204 macrocharcoal samples for this interval. A total
197 of 162 samples for palynofacies and 200 microcharcoal samples are included in the LPE study
198 interval.

199 Rock samples of 10–30 g weight were split into 0.5 cm³ fragments to minimize the breakage of the
200 organic particles whilst optimizing the surface area for palynological acid maceration. First, the 190
201 samples were treated with 10 % and 37 % HCl to remove carbonate. After this, hydrofluoric acid (40
202 % HF) was added to remove silicates from the sample. The samples were left to digest for 48 h, after
203 which cold concentrated HCl (37 %) was added to avoid calcium fluoride precipitation. Each sample
204 was left to settle, after which it could be decanted and topped up with DI water, a step that was
205 repeated ~6 times in order for the sample to neutralize.

206 After neutralizing, 5 droplets of the mixed residue were taken for the analysis of palynofacies (total
207 particulate organic matter) prior to any sieving. The remaining residue was sieved through a 125 µm
208 sieve and a 10 µm sieve to retrieve the macroscopic fraction (> 125 µm) and microscopic fraction
209 (10–125 µm). Macroscopic charcoal (>125 µm) was quantified using a Zeiss Stemi microscope, with
210 a 10 x 4 magnification lens and top lighting from a ‘goose necked’ light source. The entire
211 macroscopic fraction was dispersed in a Petri dish filled with DI water and the number of charcoal
212 particles counted and expressed per 10 g of processed rock (n/g). In some samples large clusters of
213 matrix were not digested by the acid, in which case they were taken out and dry weighed to deduce
214 the weight of the total processed rock. Charcoal particles are identified as opaque, black, angular,
215 reflective of light, with lustrous shine, elongated, lacking brown edges, and splintering during
216 breakage, and often showing the anatomical structure of the plant preserved (SI Fig. 1 and SI Table 2,
217 Scott, 2000; Scott & Damblon, 2010).

218 Microscopic charcoal (10–125 µm) was analysed on a palynological slide. A known quantity of 125
219 µl of the microscopic fraction was mounted onto microscopic slides using glycerine jelly. A
220 transmitted light microscope (Olympus (BX53)) with a 40 x 10 magnification was used to count the
221 charcoal particles. Four transects per slide were counted, one transect on the left, two in the middle,
222 and one on the right of the coverslip. These data were then scaled up to the known quantity of the total
223 sample (Belcher et al., 2005). Palynofacies were examined to record shifts in the type of organic
224 matter (terrestrial vs marine) and potential changes in organic matter preservation and/or terrestrial
225 runoff. Palynofacies were quantified using the optical light microscope and a minimum of 300 organic
226 particles per palynological slide was counted. The types of organic matter were roughly grouped after
227 Oboh-Ikuenobe et al. (2005): terrestrial palynomorphs (spores and pollen), marine palynomorphs

228 (dinoflagellates, acritarchs, prasinophytes and foraminifera test linings), fungal remains, structured
229 phytoclasts (wood particles, parenchyma), unstructured phytoclasts (degraded plant remains),
230 charcoal, black debris (palynomorphs filled with pyrite) and amorphous organic matter (AOM: fluffy,
231 clotted and granular masses, colour ranging between almost colourless to yellow and pale brown).

232 XRD clay mineralogy

233 A total of 55 samples were prepared for clay mineralogy spanning the SPB interval and 194 samples
234 for the LPE interval. About 5 g of bulk-rock sample was gently crushed and powdered with an agate
235 mortar, after which about 2–3 g of the powdered sample was decarbonated with a 0.2 M HCl solution.
236 The samples were left to settle for 95 min, after which the suspended clay sized fraction (< 2 µm) was
237 extracted with a syringe (following Stokes' law). The clay fraction was centrifuged and subsequently
238 smeared and oriented on glass slides. The samples were analysed by X-ray diffraction (XRD) using a
239 Bruker D4 Endeavour diffractometer (Bruker, Billerica, MA, USA) with Cu K α radiations, LynxEye
240 detector and Ni filter under 40 kV voltage and 25 mA intensity at the Biogéosciences Laboratory,
241 Université Bourgogne/FrancheComté, Dijon. Three runs were performed per sample to discriminate
242 the clay phases: (1) air-drying at room temperature; (2) ethylene-glycol solvation for 24 h; (3) heating
243 at 490 °C for 2 h, following Moore & Reynolds (1997). Comparing the three diffractograms obtained,
244 the clay minerals were identified using their main diffraction (d0001) peak. The proportions of each
245 clay mineral on glycolated diffractograms was estimated with the MACDIFF 4.2.5 software
246 (Petschick, 2000). The identification of the clay minerals further follows the methods in Moore &
247 Reynolds (1997) and Deconinck et al. (2019).

248 Statistical analysis

249 Orbital filters and the charcoal record

250 The Pliensbachian of the Mochras core has a well-established astrochronological framework (Ruhl et
251 al., 2016; Hinnov et al., 2018; Storm et al., 2020; Hollaar et al., 2021; Pienkowski et al., 2021). Based
252 on the existing cyclostratigraphy, the 100 kyr eccentricity cycle lies within the range of 3.2–10.2 m
253 (Ruhl et al., 2016; Hinnov et al., 2018), 6.3–4.8 m (Storm et al., 2020), and ~5.3 m (Pieńkowski et al.,
254 2021) for the here studied SPB and LPE intervals. These intervals each compromise ~7–8 short
255 eccentricity cycles. No spectral analysis has been performed on the records presented here because of
256 the limited time span represented. Instead, we compare the charcoal and clay records visually with the
257 100 kyr and 405 kyr filters based on Ca and Ti (Ruhl et al., 2016; Hinnov et al., 2018). In SI Fig. 2 we
258 overlay the 3.2 – 10 m filter (based on Ruhl et al., 2016) derived from the macrocharcoal record with
259 the normalized dataset of the macrocharcoal record.

260 Pearson correlation

261 A Pearson correlation was used to test for possible correlation between the charcoal abundance (both
262 size fractions) and palynofacies and the significance using RMatlab2021b. The p value tests the

263 hypothesis of no correlation against the alternative hypothesis of a positive or negative correlation,
264 with the significance level at $\alpha = 0.05$. See SI Fig. 3.

265 Wilcoxon test

266 A Wilcoxon rank sum test was performed in RMatlab2023b to test the null hypothesis of equal means
267 between the charcoal populations of the LPE and the SPB interval with the significance level at $\alpha =$
268 0.05. The test is performed for the macrocharcoal and microcharcoal records separately.

269 PCA analysis

270 Principal component analysis (PCA) was performed to explore the potential covariance of charcoal,
271 clay mineralogy, palynofacies and mass-spectrometry records for the two studied intervals. This was
272 executed in the software PAST (Hammer et al., 2001) on the normalized dataset (macrocharcoal,
273 microcharcoal, TOC, CaCO_3 , $\delta^{13}\text{C}_{\text{org}}$, S/I, Sm/K, K/I, phytoclasts).

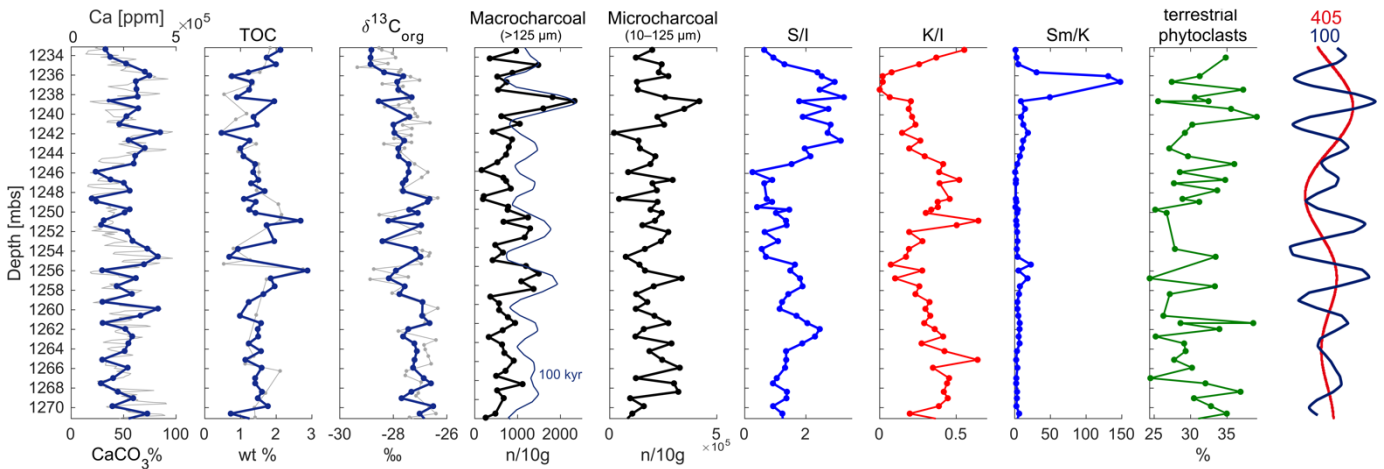
274 **3 Results**

275 The data presented here that cover the run-up to and onset of the SPB (1271–1233 mbs) show a ~ 1.8
276 ‰ negative shift in $\delta^{13}\text{C}_{\text{org}}$ spanning the end of the negative CIE limb in the Mochras borehole and
277 reaching most negative values. The results of the LPE interval which encompass the run-up and onset
278 of the LPE (951 – 918 mbs), show a rapid positive shift in the $\delta^{13}\text{C}_{\text{org}}$ of ~ 1.8 ‰ (between 930.8 –
279 930.4 mbs) (in agreement with Storm et al., 2020).

280 Large fluctuations are observed in the abundance of both macroscopic ($>125 \mu\text{m}$) and microscopic
281 ($10\text{--}125 \mu\text{m}$) fossil charcoal for both CIEs. For the SPB, microcharcoal abundance fluctuates from
282 $2 \times 10^4\text{--}4.2 \times 10^5$ (mean 2×10^5) particles per 10 g of sediment, and the number of macrocharcoal
283 particles varies from 99–2327 (mean 787) particles per 10 g sediment (Fig. 2, SI Table 3). A similar
284 trend is observed in both size fractions, with individual charcoal peaks fluctuating on a 2–4 m scale
285 (Fig. 2). In the higher resolution LPE interval, metre-scale individual peaks of charcoal abundance are
286 observed, with microcharcoal abundance fluctuating from $4.5 \times 10^3\text{--}4.3 \times 10^5$ (mean 1.1×10^5) particles
287 per 10 g of sediment, and the number of macrocharcoal particles varies from 8–2276 (mean 376)
288 particles per 10 g sediment (Fig. 3, SI Table 3). Longer term fluctuations in the macrocharcoal record
289 are also observed, with bundling of peaks visible every $\sim 4\text{--}5$ m. Micro- and macro-charcoal are more
290 abundant in the SPB compared to the LPE (Fig. 4). The outcome of the Wilcoxon signed rank test
291 confirms a different median of the SPB and LPE macrocharcoal (H_0 rejected, $p < 0.001$) and

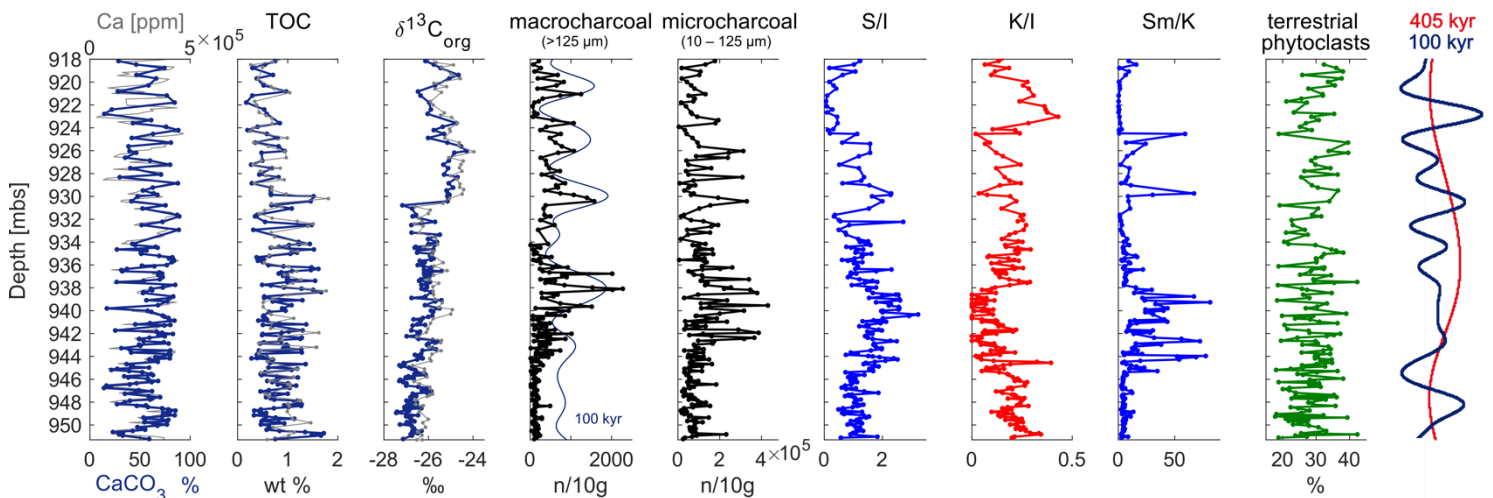
292 microcharcoal (H0 rejected, $p < 0.001$).

293



294 **Fig. 2: The SPB studied interval showing all proxies of this study in context of the orbital filters**
295 **(Ruhl et al., 2016).** The CaCO_3 , TOC and $\delta^{13}\text{C}_{\text{org}}$ (blue) data obtained for the present study are
296 plotted over previously published data (light grey – Ruhl et al., 2016; Storm et al., 2020). The
297 macrocharcoal abundance shows ~8 increases and decreases throughout the studied interval. These
298 high-low intervals in the macrocharcoal record correspond to the 100 kyr filter (blue; and see SI Fig.
299 2). The majority of macrocharcoal peaks are mirrored in the microcharcoal fraction. Alternating
300 phases of increase in the smectite/illite ratio (S/I) and the kaolinite/illite ratio (K/I) indicate swings in
301 the hydrological cycle. This is further indicated by the smectite/kaolinite ratio (Sm/K). The percentage
302 of terrestrial phytoclasts shows that the terrestrially sourced organic particles fluctuate around 30%
303 in the studied interval. Finally, the bandpass-filtered time series of the Ca-elemental XRF record of
304 Ruhl et al. (2016) indicate that the clay records shift dominance on a 405 kyr time scale. The peaks in
305 the macrocharcoal record occur on a 100 kyr time scale (see also SI Fig. 2).

306

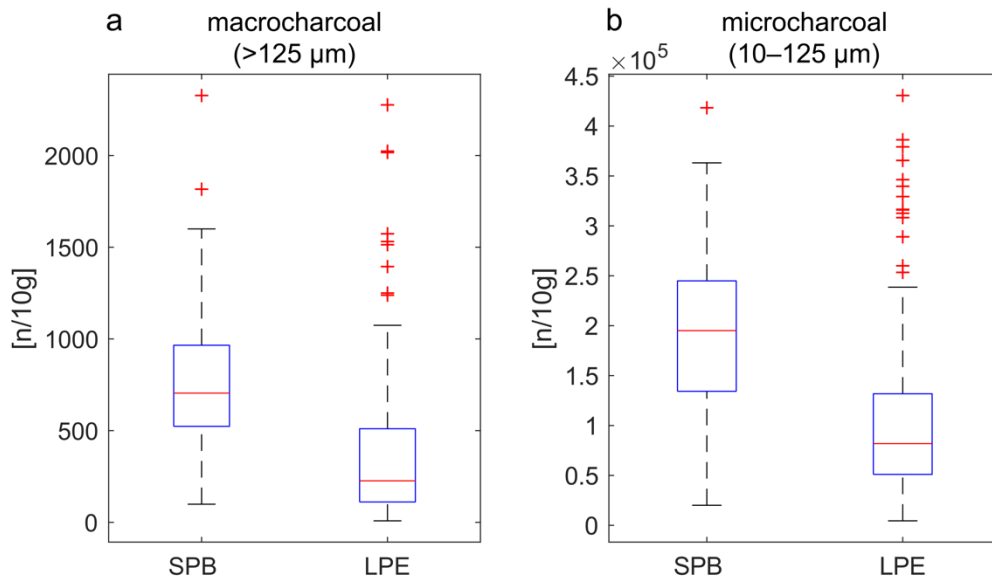


307 **Fig. 3: Synthesis of the LPE interval showing all proxies considered in this study in context of the**

308 *orbital filters (Ruhl et al., 2016). The CaCO₃, TOC and $\delta^{13}C_{org}$ (blue) from Hollaar et al. (2023) are*
309 *plotted over independently generated data (light grey - Ruhl et al., 2016; Storm et al., 2020). The*
310 *macrocharcoal abundance shows ~7 peaks throughout the studied interval. These 7 increases and*
311 *decreases in macrocharcoal abundance correspond to the 100 kyr eccentricity (in blue, see SI Fig. 2).*
312 *The majority of macrocharcoal peaks are mirrored in the microcharcoal fraction. Alternating phases*
313 *of increase in the smectite/illite ratio (S/I) and the kaolinite/illite ratio (K/I) indicate swings in the*
314 *hydrological cycle. This is further indicated by the smectite/kaolinite ratio (Sm/K). The percentage of*
315 *terrestrial phytoclasts shows that the terrestrially sourced organic particles fluctuate around 30 % in*
316 *the studied interval. Finally, the orbital filters of Ruhl et al. (2016) are placed next to the proxy*
317 *records. This shows that the clay records shift dominance on a 405 kyr time scale. The peaks in the*
318 *macrocharcoal record occur on a 100 kyr time scale.*

319

320 The palynofacies of both intervals is typically marine (AOM>58%). The proportion of terrestrial vs
321 marine organic matter remains relatively stable through both the SPB and LPE, varying between 24.4
322 and 39.1% (mean 30.7%), and 17.7 and 42.3% (mean 28.9%), respectively. Charcoal accounts for
323 ~3.7% and ~4.5% of the total particulate organic matter, respectively for the SPB and the LPE
324 intervals (SI Fig. 4). The abundance of macrocharcoal is not influenced by the percentage of terrestrial
325 particulate organic matter through the SPB and LPE intervals (SPB $r = -0.12$, $p = 0.42$; LPE $r = 0.06$,
326 $p = 0.46$) and nor is the microcharcoal abundance for the SPB interval ($r = 0.07$, $p = 0.62$). However, a
327 very weak correlation exists between the percentage of terrestrial phytoclasts and microcharcoal
328 abundance in the LPE interval ($r = 0.16$, $p = 0.05$). These results suggest that the preservation and/or
329 influx of terrestrial particulate organic matter is not the main driver of fluctuations in charcoal
330 abundance.



331

332 **Fig. 4:** Distribution boxplots of the macrocharcoal and microcharcoal abundance of the SPB and
 333 LPE studied intervals. (a) Average macrocharcoal abundance is higher in the SPB interval compared
 334 to the LPE interval, however, the absolute minimum and maximum are similar. (b) Average
 335 microcharcoal abundance is higher for the SPB compared to the LPE. The minimum number of
 336 microcharcoal particles is lower for the LPE, however, the maximum microcharcoal abundance is
 337 similar in both records.

338

339 The clay mineral assemblages of the SPB and LPE are dominated by illite, kaolinite and smectite (I-S
 340 R0), with smectite increasing in parallel with decreases of illite and kaolinite (SI Fig. 5). Low
 341 proportions of chlorite and sparse I-S R1 are present in the SPB record. Chlorite and I-S R1 are
 342 generally low in the LPE record but increase between 924–219 mbs (SI Fig. 5). Two smectite-
 343 enhanced phases occur for the SPB, at 1264–1255 mbs and 1245–1235 mbs. Both these phases are
 344 coeval with high charcoal abundance (both size fractions) (Fig. 2, SI Fig. 6). Additionally, the LPE
 345 interval encompasses two stratigraphic intervals rich in smectite; from 944–937 mbs and 931–924
 346 mbs. Charcoal abundance (both size fractions) increases overall, and coevally with the S/I, over ~5 m
 347 scale fluctuations, and decreases at levels with high K/I (Fig. 3, SI Fig. 7). The 3.2–10.2 m orbital
 348 filter of the macrocharcoal records (interpreted as the 100 kyr eccentricity (Ruhl et al., 2016; Hinnov
 349 et al., 2018; Storm et al., 2020; Pienkowski et al., 2021)), indicates that the observed fluctuations in
 350 the macrocharcoal record occur with a 100 kyr periodicity (SI Fig. 2).

351

352 4 Discussion

353 *Charcoal transport and preservation*

354 The charcoal records for both the SPB and LPE intervals do not appear to be linked to the terrestrial
355 influx of materials, as evidenced by the palynofacies. No correlation or covariance exists between the
356 abundance of terrestrial phytoclasts and the number of charcoal particles, which suggests that the
357 abundance of charcoal is not a reflection of preservation and/or runoff changes. Inferred sea level
358 changes during the LPE and the SPB could potentially have impacted the charcoal abundance record
359 and the clay mineralogy. Transgression and relative sea-level rise during the SPB has been extensively
360 recorded from the Boreal and Tethys regions, and from South America (e.g. Legarreta and Uliana,
361 1996; de Graciansky et al., 1998; Hesselbo & Jenkyns, 1998; Danisch et al., 2019; Silva et al., 2021).
362 The Late Pliensbachian is characterized by widespread regressive facies and inferred relative sea-level
363 fall, likely indicating a closer proximity to shore also in the Mochras borehole. Fossil wood in the
364 Mochras borehole has been shown to become more abundant at this time, suggesting a potential bias
365 of higher terrestrial input from a nearby landmass (Ullmann et al., 2022). However, the mean
366 abundance of macrocharcoal and microcharcoal is higher during the SPB (mean of 787 and 2×10^5
367 respectively) compared to the LPE (mean of 376 and 1.1×10^5 respectively) in the Mochras borehole,
368 suggesting that the shore proximity did not impact overall charcoal abundance. Similarly, the
369 palynofacies analysis indicates that the mean abundance of terrestrial particulate organic matter during
370 the SPB (30.7%) is not higher compared to the LPE (28.9%). Hence, we take this as strong evidence
371 that the record of fossil charcoal records changes in wildfire activity.

372 *Orbital forcing of the hydrological cycle and fire*

373 Alternations in the dominance of smectite and kaolinite occur approximately every 10 m in both the
374 LPE and SPB records. Kaolinite and smectite reflect hydrological changes in the palaeoenvironment
375 of the Cardigan Bay Basin (Deconinck et al., 2019; Munier et al., 2021). As the smectite and kaolinite
376 clay minerals are detrital in character and their abundance varies in opposition to one another (Fig. 2
377 and 3), these clays are likely derived from pedogenic weathering profiles (Deconinck et al., 2019).
378 Smectite preferentially forms under a warm and seasonally arid climate, similar to a monsoonal
379 climate system or the winter-wet climate of the Mediterranean zone (Chamley, 1989; Deconinck et al.,
380 2019). Kaolinite is indicative of an accelerated hydrological cycle and an intensification of hydrolysis,
381 increased runoff and a year-round wet climate (Chamley, 1989; Ruffell et al., 2002) either via
382 formation in strong weathering profiles or via the physical erosion of kaolinite-bearing rocks
383 (Chamley, 1989). Pedogenic kaolinite preferentially forms in a hot climate (Chamley, 1989; Ruffell et
384 al., 2002). At times of high smectite abundance, fire activity is greatest as observed from the macro-
385 and micro-scopic charcoal fractions (Fig. 2 and 3). Based on the astrochronological framework of the
386 Mochras borehole (Ruhl et al., 2016; Hinnov et al., 2018; Storm et al., 2020; Pieńkowski et al., 2021)
387 these alternations appear to occur in concert with the 405 kyr long-eccentricity cycles (Fig. 2, Fig. 3).
388 Eccentricity modulates the precession driven changes in seasonal and latitudinal distribution of
389 insolation (Imbrie & Imbrie, 1980; Berger et al., 1989). One ~20 kyr precession cycle can represent a

390 strongly seasonal extreme climate for ~10 kyr and a weakly seasonal climate for the subsequent ~10
391 kyr. The geological record averages the amplification or suppression of seasonality between years (SI
392 Fig. 8). Eccentricity forcing modulates the amplitudes of these extremes in seasonality with
393 periodicities of 100 kyr and 405 kyr.

394 In the Mesozoic, eccentricity maxima are commonly associated with dry climates that are disrupted
395 by short and intense periods of precipitation and storm activity in the boreal landmasses bordering the
396 NW Tethys (Martinez & Dera, 2015). In contrast, eccentricity minima are characterized by a more
397 moderate seasonal contrasts and year-round wet conditions (Martinez & Dera, 2015). Eccentricity
398 minima are linked to periods of enhanced runoff and weathering conditions as evidenced by high
399 kaolinite content, $^{87}\text{Sr}/^{86}\text{Sr}$, and negative shifts in $\delta^{18}\text{O}$ (Martinez & Dera, 2015). Therefore, we link
400 the observed smectite-rich intervals to eccentricity maxima and the kaolinite-rich intervals to
401 eccentricity minima. Charcoal abundance is highest during the seasonal climate of the eccentricity
402 maxima for the SPB (Fig. 2 and 3), in agreement with the previous findings for the LPE (Hollaar et
403 al., 2021, 2023).

404 Both the LPE and SPB study intervals span two 405-kyr cycles (Ruhl et al., 2016; Hinnov et al., 2018;
405 Storm et al., 2020; Pieńkowski et al., 2021). The relative abundance of smectite and the abundance of
406 charcoal both reach a peak during the maxima in the long eccentricity cycle, supporting the notion
407 that orbitally driven changes in seasonal contrast in hydrolysis led to high fire activity. Within these
408 long-term trends, the macrocharcoal record also shows ~5 m scale individual peaks or clusters in both
409 the LPE and SPB records (SI Fig. 2, Fig. 2 and 3). Based on the existing age model (Ruhl et al., 2016;
410 Hinnov et al., 2018; Storm et al., 2020; Pieńkowski et al., 2021) we derive that this is the expression
411 of the ~100 kyr eccentricity cycle in the macrocharcoal record. The bandpass-filtered time series
412 representing the ~100 kyr cycle in the Pliensbachian of the Mochras core (derived from the Ca and
413 macrocharcoal records), captures the observed ~5 m oscillations in the fire record (SI Fig. 2, Fig. 2
414 and 3) (Ruhl et al., 2016; Hinnov et al., 2018; Storm et al., 2020; Pieńkowski et al., 2021).

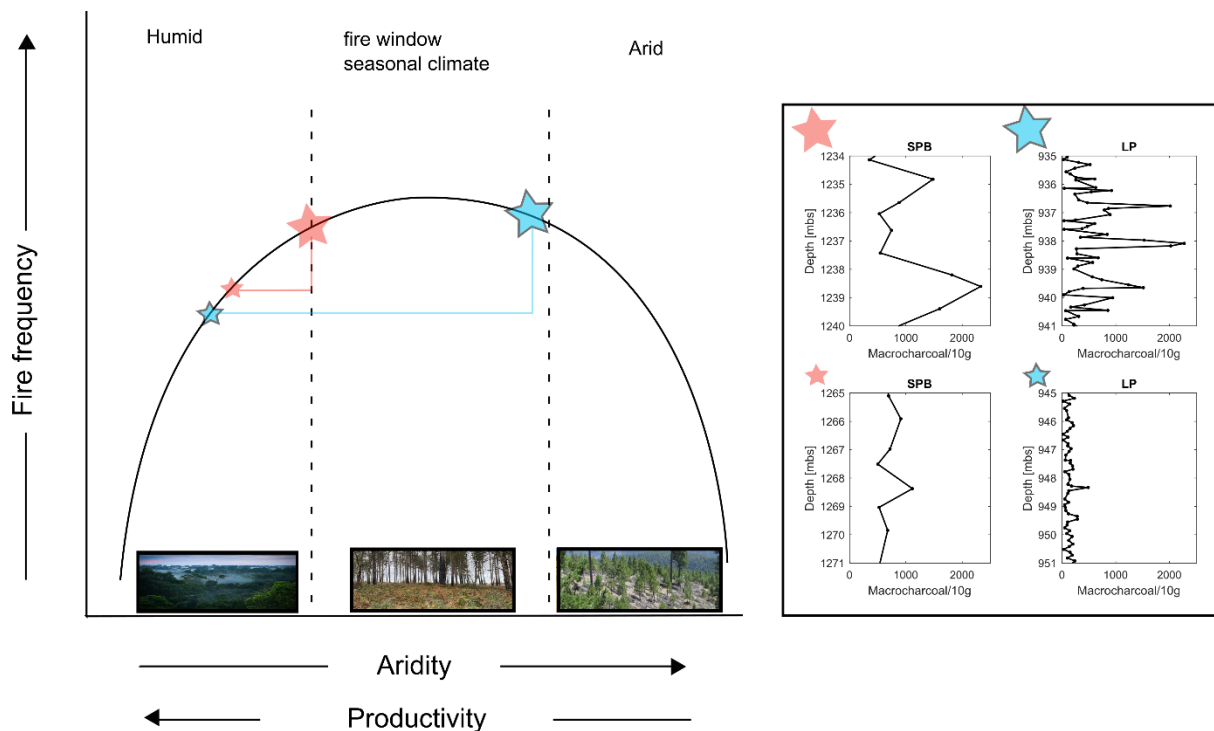
415 The Sinemurian–Pliensbachian transition is generally associated with an overall warm and humid
416 climate (Korte & Hesselbo, 2011; Gómez et al., 2016), and enhanced levels of runoff and weathering
417 (Bougeault et al., 2017). The results presented here suggest that within this overall warm and humid
418 background, orbital forcing created year-round wet periods, that were not conducive to frequent fire,
419 alternating with periods that remained warm but had a more seasonal climate, that allowed ignition
420 during the dry season. In contrast, the LPE, and the sediments of late *Margaritatus ammonite*
421 chronozone formed in an overall semi-arid climate with proposed lower runoff levels from the land
422 into the sea (Deconinck et al., 2019; Hollaar et al., 2021; 2023). During the run-up of the LPE we
423 infer orbitally forced alternating climatic states of more extreme seasonality (high fire and smectite)
424 and a more equitable year-round wet climate (low fire and high kaolinite) (Hollaar et al., 2021; 2023)

425 acting within this overall semi-arid climate phase. Overall, kaolinite fluctuates in abundance in
426 opposition to smectite, reflecting hydrological changes from wet and hot to semi-arid and hot, in
427 agreement with high fire activity during a seasonal climate and fire suppression during a year-round
428 wet climate for both the LPE and the SPB.

429 *Vegetation, fire and the intermediate fire-productivity gradient*

430 Fuel (vegetation biomass) and moisture status of the fuel, as governed by seasonal patterns in
431 precipitation and temperature, are the core factors that influence fire behaviour and fire regime
432 (Archibald et al., 2009; Cochrane & Ryan, 2009; Bradstock, 2010; Archibald et al., 2013; Bowman et
433 al., 2014; Archibald et al., 2018). Ecosystems with limited wildfire activity are generally associated
434 with either high precipitation and abundant primary productivity, or low productivity under strongly
435 arid conditions (Pausas & Paula, 2012). In contrast, high wildfire activity occurs in climates that are in
436 the middle of the productivity gradient, where during moist periods plant growth is rapid and biomass
437 builds up forming a connected fuel structure. When followed by periods of drought the fuel moisture
438 content is lowered enabling fire ignition and spread (Pausas & Paula, 2012). Additionally, higher
439 sensitivity to fuel moisture levels in the tropical or mesic areas have been noted, where a small fall in
440 fuel moisture content can lead to more flammable conditions (Cochrane, 2003). Such that the mid
441 points in the intermediate fire-productivity gradient are further enhanced. The intermediate fire-
442 productivity hypothesis (Pausas & Bradstock, 2007; Pausas & Ribeiro, 2013) conceptualizes this
443 relationship between climate-vegetation-fire, where fire activity is plotted along an aridity and
444 productivity gradient (Fig. 5). The observed alternating modes of high and low fire activity, as
445 inferred from the lower Jurassic fossil charcoal record, during the onset of the SPB and LPE, likely
446 indicates shifts in seasonality of the Cardigan Bay Basin hinterland and would place both the LPE and
447 the SPB at intermediate productivity levels during maximum eccentricity forcing. The deep time
448 combined fire and hydrological records we present here are in agreement with the intermediate
449 productivity hypothesis of Pausas & Bradstock (2007) and indicate that even the very different plant
450 functional types and different vegetation assemblages, e.g., a world without grasses, were still subject
451 to this overall fire-productivity gradient control. We indicate on Fig. 5 how these ecosystems without
452 grasses and other flowering plants may have looked in respect to typical Jurassic fuel compositions.
453 We suggest that both the LPE and the SPB switched between a state of low fire (either limited by
454 climatic aridity or the presence and presence and connectivity of fuel) and a state of high fire during
455 which seasonal contrast is high and an ideal ‘fire window’ exists in which biomass built up during the
456 wet season after which a fire-prone season followed (Fig. 5).

457



458

459 **Fig. 5: The LPE and SPB fire records placed on the intermediate productivity gradient.** The graph
 460 is adapted from Pausas & Bradstock (2007). Fire frequency is highest in the middle of the hyperbola,
 461 medium levels of aridity and productivity created a seasonal climate in which seasonal biomass
 462 growth was possible (productivity) and seasonally the fuel moisture limits were lower in a season of
 463 drought (aridity), this created the optimized 'fire window'. The SPB is plotted on this fire-productivity
 464 gradient in red: the small star indicates the eccentricity minimum state and the large star the
 465 eccentricity maximum state. The LPE is plotted on the fire-productivity gradient in blue, and again the
 466 small star indicates the eccentricity minimum and the large star the eccentricity maximum. The LPE
 467 has a larger range compared to the SPB, and experienced more fire suppression due to high humidity
 468 levels during eccentricity minima, and also was closer to a productivity limitation state during the
 469 eccentricity maximum.

470 The studied Early Jurassic time-interval likely had five distinct biomes; a seasonal dry (summerwet or
 471 subtropical) biome in the low latitudes, a desert biome in the subtropics, narrow latitudinal bands of a
 472 winterwet biome at low-mid latitude, and warm temperate and cool temperate biomes at mid- and
 473 high-latitudes, respectively (Rees et al., 2000; Willes and McElwain, 2014). The Cardigan Bay Basin
 474 was likely positioned within the winterwet biome at approximately 35 °N (Torsvik et al., 2017). It
 475 therefore would have sat within the bounds of the fire window of the intermediate fire-productivity
 476 hypothesis (Fig. 5). The winterwet biome in both the Sinemurian and Pliensbachian stages were
 477 dominated by conifers as the canopy tree, with a mid-canopy vegetation of cycads and tree-ferns, and
 478 an understory mixture of seed ferns, horsetails and ferns that likely flourished during wetter periods
 479 (Rees et al., 2000; Slater et al., 2019; Bos et al., 2023). This is evidenced from sporomorph data from
 480 the Mochras borehole that hosts abundant fossil pollen in the Sinemurian and Pliensbachian (>94%)

481 (Van de Schootbrugge et al., 2005). Additionally, nearby locations also show evidence of orbitally
482 paced shifts in vegetation assemblages from sites at St. Audries Bay, UK and in NW Germany (Bonis
483 et al., 2010; Bos et al., 2023).

484 During the 100 kyr eccentricity maxima in the UK pollen from the dry-adapted cheirolepidacean
485 conifers is found to be highly abundant (Bonis et al., 2010). Whilst, in Germany a mire-conifer
486 community is apparent with sporomorphs indicating variations in abundance of ferns and fern allies
487 occurring over a 405-kyr eccentricity cycle, with ferns most abundant during eccentricity maxima
488 (Bos et al., 2023).

489 Dry-adapted vegetation, such as the cheirolepidacean conifers likely thrived during more extreme
490 seasonal droughts, maintaining their biomass. In contrast, ferns and fern allies, and mire-conifers as
491 humid-loving plants would grow rapidly during sustained, year-round, periods of rainfall (eccentricity
492 minima), likely inhabiting both open environments and colonising the understory of conifer forests.
493 Furthermore, these humid-loving plants would also be able to build dense connected fuel loads during
494 the wet-season of eccentricity maxima, that were then readily dried during the annual dry-season.
495 Ferns, when cured, carry high intensity fires (Adie et al., 2011; Belcher and Hudspith, 2016) and
496 during the Mesozoic ‘fern prairies’ have been linked to intense surface fires (Harris, 1981; Van
497 Konijnenburg-Van Cittert, 2002; Collinson et al., 2007, 2009). Hence, they are suggested to have
498 functioned in a similar fashion to support fires as grasslands and fern stands do today; Mesozoic fern
499 prairies and savannahs therefore likely filled a similar ecological niche to grasses in the modern day
500 (Belcher, 2013 and references therein). Ferns are indeed a common feature of Mesozoic charcoal
501 assemblages, showing their association with fire throughout time (e.g. Collinson et al., 2000; Brown
502 et al., 2012).

503 In the present-day, temperature is an important regulator of fire occurrence. Whilst dead fuel moisture
504 (e.g. that of litter and cured herbaceous components) is primarily influenced by the variability in
505 relative humidity, live fuels are controlled by the combination of temperature and moisture
506 availability, where long periods of drought or heat wave extremes can strongly influence the
507 flammability of live fuels. Sea surface temperatures during the Sinemurian and Pliensbachian were at
508 times apparently higher than 28 °C (Robinson et al., 2017). But high-resolution temperature
509 reconstructions are lacking for the Early Jurassic. Orbital forcing of regional–global seawater
510 temperatures occurred throughout the Cenozoic (Westerhold et al., 2020), and likely also the
511 Mesozoic; however, the climate response to changes in orbital insolation is non-linear, and the mean
512 annual insolation is not impacted by precession (Rubicam, 1994). Therefore, the biomes of the SPB
513 not only existed in an overall warm world that was characterized by background orbitally driven
514 climate shifts across the moister side of the fire-productivity gradient, but superimposed on this live
515 fuels were also responsive to extreme weather linked to periods of drought and heat.

516

517 We propose that the overall humid climate of the SPB fits the high productivity scenario, in which the
518 frequency of flammable conditions is the main factor controlling fire occurrences. No evidence was
519 found to place the SPB on the productivity-limiting high-aridity side of the fire-productivity gradient,
520 where fire frequency would have been mainly influenced by enhanced rainfall in an otherwise dry
521 climate. These findings are in line with the presence of plant cuticle through the studied record,
522 indicating the presence of vegetation throughout this time period and during both phases of high and
523 low modes of fire activity. Hence, the SPB seems to conform to the humid and high productivity end
524 of the aridity gradient (Fig. 5 red lines). Within these constraints (Fig. 5) the SPB is characterized by
525 likely two states across the fire productivity gradient. The biome was situated at the wetter, low fire
526 side of the fire-productivity gradient during eccentricity minima (Fig. 5), and at the seasonal, high fire
527 end of the fire-productivity gradient during eccentricity maxima (but only for each precession half-
528 cycle) (Fig. 5).

529 The fluctuations detected in the present study for the SPB occurred over both long-eccentricity and
530 short eccentricity timescales in the macrocharcoal record, showing longer phases of overall
531 enhancement of fire (405 kyr eccentricity) and relatively abrupt shifts from low to high fire and back
532 again (~100 kyr eccentricity). For this reason, the SPB is placed on a steep portion of the fire-
533 productivity gradient curve (Fig. 5). Overall, the mean charcoal abundance is relatively high, and no
534 sustained periods of very low charcoal abundance are observed in the SPB record, which indicates
535 that the climate never became too wet to fully limit fire activity at that time.

536 The Late Pliensbachian has been linked to a global cooling event, with a potential of 5–7 °C lowering
537 in temperature inferred for the NW Tethys region (Korte et al., 2015). The atmospheric moisture
538 holding capacity of a cooler climate is lower compared to a warm climate, in which a 1 °C cooling
539 likely lowers the water holding capacity of air by 7% (Trenberth et al., 2005). The presence of
540 terrestrial phytoclasts throughout confirms the presence of vegetation in the surrounding landmasses
541 throughout this period. The mean abundance of charcoal for the LPE section is slightly lower than that
542 of the SPB and the lowest charcoal abundances are coeval with a K/I enhancement, suggesting that
543 during eccentricity minima environmental conditions moved further into the humid zone of the fire-
544 productivity gradient (Fig. 5 blue line). Increasing eccentricity shifted the system to a more seasonal
545 climate where the fire and clay records indicate the presence of a wet season that allowed for build-up
546 of biomass followed by a dry season in which fire was able to be ignited and spread.

547 Conceptually, the relatively drier and cooler LPE climate would have resulted in conditions that are
548 more arid, shifting to the biomass-limited part of the productivity/aridity – fire frequency gradient
549 during eccentricity maxima, compared to the SPB (Fig. 5 blue lines). This is supported by the large
550 fluctuations observed between low fire frequency and high fire frequency for the LPE and the fact that

551 estimated high fire periods did not occur suddenly, but rather were sustained over a larger part of the
552 cycle. Therefore, the phase of highest fire frequency operating in the seasonal ‘fire window’ as
553 indicated in figure 5 for the LPE (blue lines) likely occurred for a larger part of the fire productivity
554 gradient. Hence, conditions across the LPE occurred across a wider range of the productivity/aridity
555 and fire frequency gradients (Fig. 5 blue lines) compared to the SPB. There is no evidence that
556 conditions ever became limited by aridity, and conditions during the LPE did not extend beyond the
557 seasonal fire window into the arid part of the productivity/aridity gradient.

558 Importantly, the Jurassic climate was overall warm and humid, about 5–10 °C warmer on global
559 average compared to today (e.g., Rees et al., 2000; Sellwood & Valdes, 2008), with ~3.5–10 times the
560 pre-industrial value of atmospheric $p\text{CO}_2$ during the Early Jurassic (e.g. Retallack, 2001; Beerling &
561 Royer, 2002; McElwain et al., 2005; Berner, 2006; Steinthorsdottir & Vajda, 2015; Li et al., 2020). In
562 this context, it may not be surprising that a relative cooling event in the Early Jurassic did not lead to
563 the aridity and biomass-limiting conditions observed during the last glacial period, at latitudes of ~38
564 °C N (Daniau et al., 2007).

565 **5 Conclusions**

566 The study of two different climatic ‘background’ states, at the LPE and the SPB, shows that fire
567 activity was strongly modulated by orbital eccentricity cycles. The 405 kyr shifts in the record of
568 wildfire prevalence reflect similar changes also in the hydrological cycle (based on clay mineralogy
569 data) showing that high fire activity occurred during periods of high seasonal contrast and that fire
570 activity was suppressed during periods of high year-round humidity, because the latter would have
571 enhanced the fuel moisture levels and prevented frequent ignition and sustained fire spread. The fire
572 record of both climatic events is limited by the high fuel moisture levels during eccentricity minima,
573 but fires were more prevalent during times of increased seasonality, every precession half-cycle
574 during eccentricity maxima. Hence, during both events fire activity was limited by fuel moisture
575 content and not by productivity. Both the SPB and the LPE climate systems were therefore situated on
576 the moisture-limited side of the intermediate fire-productivity gradient (Fig. 5). Due to the lower
577 moisture-holding capacity of cold air, the overall higher seasonality of the Late Pliensbachian and the
578 more sustained high fire-frequency periods (based on the charcoal record for the LPE) we place the
579 LPE towards the higher end of the aridity gradient, within maximum seasonality and maximum fire
580 frequency window of the fire productivity graph (Fig. 5). The SPB fire regime reflected a more humid
581 climate that shifted abruptly between low fire frequency to high fire frequency within less extreme
582 bounds on the aridity gradient. This research reveals that the intermediate-fire productivity hypothesis
583 (Pausas & Bradstock, 2007) can also be applied to high-resolution deep time records, before the
584 evolution of grasses and that this hypothesis explains well the influence of orbital cycles within
585 different overall climate states, be they cooling or warming trends. The coupling of high-resolution
586 clay mineralogy and fossil charcoal records, combined with constraints on orbital forcing at such

587 time, allows for inferences on how Earth's natural climate state variability has driven shifts in
588 terrestrial productivity through the geological past.

589 **Acknowledgements**

590 This is a contribution to the JET project funded by the Natural Environment Research Council
591 (NERC) (grant number NE/N018508/1). All authors acknowledge funding from the International
592 Continental Scientific Drilling Program (ICDP) and TPH acknowledges funding from the University
593 of Exeter.

594 **Conflict of Interest**

595 The authors declare no conflicts of interest relevant to this study.

596 **Data Availability Statement**

597 Supplementary data are available at the National Geoscience Data Centre at Keyworth (NGDC)
598 at <https://doi.org/10.5285/1461dbe5-50a8-425c-8c49-ac1f04bcc271> (Hollaar, 2022) for the interval
599 934–918 m. b.s. All data presented for the interval 951–934 m. b.s. are available at the National
600 Geoscience Data Centre at Keyworth (NGDC) at [https://doi.org/10.5285/d6b7c567-49f0-44c7-a94c-
601 e82fa17ff98e](https://doi.org/10.5285/d6b7c567-49f0-44c7-a94c-e82fa17ff98e) (Hollaar et al., 2021b). All data for the interval 1271–1233 mbs is deposited at the
602 University of Exeter: <http://hdl.handle.net/10871/133255>.

603 **Supporting Information**

604

605 **References**

606 Adie, H., Richert, S., Kirkman, K. P., & Lawes, M. J. (2011). The heat is on: frequent high intensity
607 fire in bracken (*Pteridium aquilinum*) drives mortality of the sprouting tree *Protea caffra* in temperate
608 grasslands. *Plant Ecology*, 212, 2013 – 2022. <https://doi.org/10.1007/s11258-011-9945-8>

609 Archibald, S., Lehmann, C. E., Belcher, C. M., Bond, W. J., Bradstock, R. A., Daniau, A. L., et al.
610 (2018). Biological and geophysical feedbacks with fire in the Earth system. *Environmental Research
611 Letters*, 13(3), 033003. <https://doi.org/10.1088/1748-9326/aa9ead>

612 Archibald, S., Lehmann, C. E., Gómez-Dans, J. L., & Bradstock, R. A. (2013). Defining pyromes and
613 global syndromes of fire regimes. *Proceedings of the National Academy of Sciences*, 110(16), 6442 –
614 6447. <https://doi.org/10.1073/pnas.1211466110>

615 Archibald, S., Roy, D. P., van Wilgen, B. W., & Scholes, R. J. (2009). What limits fire? An
616 examination of drivers of burnt area in Southern Africa. *Global Change Biology*, 15(3), 613 – 630.
617 <https://doi.org/10.1111/j.1365-2486.2008.01754.x>

618 Beerling, D. J., & Royer, D. L. (2002). Fossil plants as indicators of the Phanerozoic global carbon
619 cycle. *Annual Review of Earth and Planetary Sciences*, 30(1), 527 – 556.
620 <https://doi.org/10.1146/annurev.earth.30.091201.141413>

621 Belcher, C. M., Collinson, M. E., & Scott, A. C. (2005). Constraints on the thermal energy released
622 from the Chicxulub impactor: new evidence from multi-method charcoal analysis. *Journal of the*
623 *Geological Society*, 162(4), 591 – 602. <https://doi.org/10.1144/0016-764904-104>

624 Belcher, C. M., Collinson, M. E., & Scott, A. C. (2013). A 450-Million-Year History of Fire. In C. M.
625 Belcher (Eds.). *Fire Phenomena and the Earth System*. (pp. 240 – 241). London, UK: Wiley.

626 Belcher, C. M., & Hudspith, V. A. (2017). Changes to Cretaceous surface fire behaviour influenced
627 the spread of the early angiosperms. *New Phytologist*, 213(3), 1521 – 1532.
628 <https://doi.org/10.1111/nph.14264>

629 Berger, A., Loutre, M. F. & Dehant, V. Astronomical frequencies for pre-Quaternary palaeoclimate
630 studies. *Terra Nova* 1, 474–479 (1989). <https://doi.org/10.1111/j.1365-3121.1989.tb00413.x>

631 Berner, R. A. (2006). GEOCARBSULF: a combined model for Phanerozoic atmospheric O₂ and
632 CO₂. *Geochimica et Cosmochimica Acta*, 70(23), 5653 – 5664.
633 <https://doi.org/10.1016/j.gca.2005.11.032>

634 Bonis, N. R., Ruhl, M., & Kürschner, W. M. (2010). Milankovitch-scale palynological turnover across
635 the Triassic–Jurassic transition at St. Audrie's Bay, SW UK. *Journal of the Geological Society*, 167(5),
636 [877 – 888. https://doi.org/10.1144/0016-76492009-141](https://doi.org/10.1144/0016-76492009-141)

637 Bos, R., Lindström, S., van Konijnenburg-van Cittert, H., Hilgen, F., Hollaar, T. P., Aalpoel, H. et al.
638 (2023). Triassic–Jurassic vegetation response to carbon cycle perturbations and climate
639 change. *Global and Planetary Change*, 228, 104211. <https://doi.org/10.1016/j.gloplacha.2023.104211>

640 Bougeault, C., Pellenard, P., Deconinck, J. F., Hesselbo, S. P., Dommergues, J. L., Bruneau, L., et al.
641 (2017). Climatic and palaeoceanographic changes during the Pliensbachian (Early Jurassic) inferred
642 from clay mineralogy and stable isotope (CO) geochemistry (NW Europe). *Global and Planetary*
643 *Change*, 149, 139 – 152. <https://doi.org/10.1016/j.gloplacha.2017.01.005>

644 Bowman, D. M., Murphy, B. P., Williamson, G. J., & Cochrane, M. A. (2014). Pyrogeographic
645 models, feedbacks and the future of global fire regimes. *Global Ecology and Biogeography*, 23(7),
646 821 – 824. <https://doi.org/10.1111/geb.12180>

647 Bradstock, R. A. (2010). A biogeographic model of fire regimes in Australia: current and future
648 implications. *Global Ecology and Biogeography*, 19(2), 145 – 158. [https://doi.org/10.1111/j.1466-](https://doi.org/10.1111/j.1466-8238.2009.00512.x)
649 [8238.2009.00512.x](https://doi.org/10.1111/j.1466-8238.2009.00512.x)

650 Brown, S. A., Scott, A. C., Glasspool, I. J., & Collinson, M. E. (2012). Cretaceous wildfires and their
651 impact on the Earth system. *Cretaceous research*, 36, 162 – 190.
652 <https://doi.org/10.1016/j.cretres.2012.02.008>

653 Chamley, H. (1989). *Clay Sedimentology*. Heidelberg: Springer Berlin Heidelberg.

654 Cochrane, M. A. (2003). Fire science for rainforests. *Nature*, 421(6926), 913 – 919.
655 <https://doi.org/10.1038/nature01437>

656 Cochrane, M. A., & Ryan, K. C. (2009). Fire and fire ecology: Concepts and principles. *Tropical fire
657 ecology*, 25 – 62. https://doi.org/10.1007/978-3-540-77381-8_2

658 Collinson, M.E, Featherstone, C. Cripps, J.A, Nichols, G.J. & Scott, A.C. (2000). Charcoal-rich plant
659 debris accumulations in the Lower Cretaceous of the Isle of Wight, England. *Acta Palaeobotanica*,
660 Supplement 2, 93 – 105.

661 Collinson, M. E., Steart, D. C., Harrington, G. J., Hooker, J. J., Scob, A. C., Allen, L. O. et al. (2009).
662 Palynological evidence of vegetation dynamics in response to palaeoenvironmental change across the
663 onset of the Paleocene-Eocene Thermal Maximum at Cobham, Southern England. *Grana*, 48(1), 38 –
664 66. <https://doi.org/10.1080/00173130802707980>

665 Collinson, M. E., Steart, D. C., Scob, A. C., Glasspool, I. J., & Hooker, J. J. (2007). Episodic fire,
666 runoff and deposition at the Palaeocene–Eocene boundary. *Journal of the Geological Society*, 164(1),
667 87 – 97. <https://doi.org/10.1144/0016-76492005-185>

668 Daniau, A. L., Bartlein, P. J., Harrison, S. P., Prentice, I. C., Brewer, S., Friedlingstein, P., et al.
669 (2012). Predictability of biomass burning in response to climate changes. *Global Biogeochemical
670 Cycles*, 26(4). <https://doi.org/10.1029/2011GB004249>

671 Daniau, A. L., Sánchez-Goñi, M. F., Beaufort, L., Laggoun-Défarge, F., Loutre, M. F., & Duprat, J.
672 (2007). Dansgaard–Oeschger climatic variability revealed by fire emissions in southwestern
673 Iberia. *Quaternary Science Reviews*, 26(9-10), 1369 – 1383.
674 <https://doi.org/10.1016/j.quascirev.2007.02.005>

675 Danisch, J., Kabiri, L., Nutz, A., & Bodin, S. (2019). Chemostratigraphy of late Sinemurian–early
676 Pliensbachian shallow-to deep-water deposits of the Central High Atlas Basin: Paleoenvironmental
677 implications. *Journal of African Earth Sciences*, 153, 239 – 249.
678 <https://doi.org/10.1016/j.jafrearsci.2019.03.003>

679 Deconinck, J. F., Hesselbo, S. P., & Pellenard, P. (2019). Climatic and sea-level control of Jurassic
680 (Pliensbachian) clay mineral sedimentation in the Cardigan Bay Basin, Llanbedr (Mochras Farm)
681 borehole, Wales. *Sedimentology*, 66(7), 2769 – 2783. <https://doi.org/10.1111/sed.12610>

682 De Graciansky, P. C., Dardeau, G., Dommergues, J. L., Durllet, C., Marchand, D., Dumont, T., et al.
683 (1998). Ammonite biostratigraphic correlation and Early Jurassic sequence stratigraphy in France:
684 comparisons with some UK sections. In: de Graciansky, P.C., Hardenbol, J., Jacquin, T., Farley, M. &
685 Vail, P.R. (Eds.), Mesozoic and Cenozoic Sequence Stratigraphy of European Basins. *Special*
686 *Publication of the Society for Sedimentary Geology (SEPM)*, 60, 583 – 622.

687 Glasspool, I. J., Edwards, D., & Axe, L. (2004). Charcoal in the Silurian as evidence for the earliest
688 wildfire. *Geology*, 32(5), 381 – 383. <https://doi.org/10.1130/G20363.1>

689 Glasspool, I. J., & Gastaldo, R. A. (2022). Silurian wildfire proxies and atmospheric oxygen.
690 *Geology*. <https://doi.org/10.1130/G50193.1>

691 Gómez, J. J., Comas-Rengifo, M. J., & Goy, A. (2016). Palaeoclimatic oscillations in the
692 Pliensbachian (Early Jurassic) of the Asturian Basin (Northern Spain). *Climate of the Past*, 12(5),
693 1199 – 1214. <https://doi.org/10.5194/cp-12-1199-2016>

694 Hammer, Ø., Harper, D. A. T., Ryan, P. D. 2001. PAST: Paleontological statistics software package
695 for education and data analysis. *Palaeontologia Electronica*, 4(1): 9pp. [http://palaeo-](http://palaeo-electronica.org/2001_1/past/issue1_01.htm)
696 [electronica.org/2001_1/past/issue1_01.htm](http://palaeo-electronica.org/2001_1/past/issue1_01.htm)

697 Harris, T. M. (1981). Burnt ferns from the English Wealden. *Proceedings of the Geologists'*
698 *Association*, 92(1), 47 – 58. [https://doi.org/10.1016/S0016-7878\(81\)80019-3](https://doi.org/10.1016/S0016-7878(81)80019-3)

699 Haq, B. U. (2018). Jurassic sea-level variations: a reappraisal. *GSA today*, 28(1), 4 – 10.
700 <https://doi.org/10.1130/GSATG359A.1>

701 Hinnov, L. A., Ruhl, M. R., & Hesselbo, S. P. (2018). Reply to the Comment on “Astronomical
702 constraints on the duration of the Early Jurassic Pliensbachian Stage and global climatic fluctuations”
703 (Ruhl *et al.*, (2016). *Earth and Planetary Science Letters*, 455, 149 – 165).
704 <https://doi.org/10.1016/j.epsl.2017.10.061>

705 Hesselbo, S.P. & Jenkyns, H.C. (1998). British Lower Jurassic sequence stratigraphy. In: de
706 Graciansky, P.C., Hardenbol, J., Jacquin, T., Farley, M. & Vail, P.R. (Eds.), Mesozoic–Cenozoic
707 Sequence Stratigraphy of European Basins. *Special Publication of the Society for Sedimentary*
708 *Geology (SEPM)*, 60, 561 – 581.

709 Hollaar, T. P., Baker, S. J., Hesselbo, S. P., Deconinck, J. F., Mander, L., Ruhl, M., & Belcher, C. M.
710 (2021). Wildfire activity enhanced during phases of maximum orbital eccentricity and precessional

711 forcing in the Early Jurassic. *Communications Earth & Environment*, 2(1), 1 – 12.
712 <https://doi.org/10.1038/s43247-021-00307-3>

713 Hollaar, T. P., Hesselbo, S. P., Deconinck, J. F., Damaschke, M., Ullmann, C. V., Jiang, M., &
714 Belcher, C. M. (2023). Environmental changes during the onset of the Late Pliensbachian Event
715 (Early Jurassic) in the Cardigan Bay Basin, Wales. *Climate of the Past*, 19(5), 979-997.
716 <https://doi.org/10.5194/cp-19-979-2023>

717 Imbrie, J., & Imbrie, J. Z. (1980). Modeling the climatic response to orbital variations. *Science*,
718 207(4434), 943 – 953. <https://doi.org/10.1126/science.207.4434.943>

719 Korte, C. & Hesselbo, S. P. (2011). Shallow marine carbon and oxygen isotope and elemental records
720 indicate icehouse-greenhouse cycles during the Early Jurassic. *Paleoceanography*, 26(4).
721 <https://doi.org/10.1029/2011PA002160>

722 Korte, C., Hesselbo, S. P., Ullmann, C. V., Dietl, G., Ruhl, M., Schweigert, G., & Thibault, N. (2015).
723 Jurassic climate mode governed by ocean gateway. *Nature communications*, 6(1), 1 – 7.
724 <https://doi.org/10.1038/ncomms10015>

725 Krawchuk, M. A., & Moritz, M. A. (2011). Constraints on global fire activity vary across a resource
726 gradient. *Ecology*, 92(1), 121 – 132. <https://doi.org/10.1890/09-1843.1>

727 Legarreta, L., & Uliana, M. A. (1996). The Jurassic succession in west-central Argentina: stratal
728 patterns, sequences and paleogeographic evolution. *Palaeogeography, Palaeoclimatology,*
729 *Palaeoecology*, 120(3-4), 303 – 330. [https://doi.org/10.1016/0031-0182\(95\)00042-9](https://doi.org/10.1016/0031-0182(95)00042-9)

730 Li, X., Wang, J., Rasbury, T., Zhou, M., Wei, Z., & Zhang, C. (2020). Early Jurassic climate and
731 atmospheric CO₂ concentration in the Sichuan paleobasin, southwestern China. *Climate of the Past*,
732 16(6), 2055 – 2074. <https://doi.org/10.5194/cp-16-2055-2020>

733 Martinez, M. & Dera, G. (2015). Orbital pacing of carbon fluxes by a ~ 9-My eccentricity cycle
734 during the Mesozoic. *Proceedings of the National Academy of Sciences*, 112, 12604 – 12609.
735 <https://doi.org/10.1073/pnas.141994611>

736 McElwain, J. C., Wade-Murphy, J., & Hesselbo, S. P. (2005). Changes in carbon dioxide during an
737 oceanic anoxic event linked to intrusion into Gondwana coals. *Nature*, 435(7041), 479 – 482.
738 <https://doi.org/10.1038/nature03618>

739 Meyn, A., White, P. S., Buhk, C., & Jentsch, A. (2007). Environmental drivers of large, infrequent
740 wildfires: the emerging conceptual model. *Progress in Physical Geography*, 31(3), 287 – 312.
741 <https://doi.org/10.1177/0309133307079365>

742 Moore, D. M. & Reynolds Jr, R. C. (1997). *X-ray Diffraction and the Identification and Analysis of*
743 *Clay Minerals*. Oxford: Oxford University Press.

744 Munier, T., Deconinck, J. F., Pellenard, P., Hesselbo, S. P., Riding, J. B., Ullmann, C. V., et al.
745 (2021). Million-year-scale alternation of warm–humid and semi-arid periods as a mid-latitude climate
746 mode in the Early Jurassic (late Sinemurian, Laurasian Seaway). *Climate of the Past*, 17(4), 1547 –
747 1566. <https://doi.org/10.5194/cp-17-1547-2021>

748 Oboh-Ikuenobe, F. E., Obi, C. G. & Jaramillo, C. A. (2005). Lithofacies, palynofacies, and sequence
749 stratigraphy of Palaeogene strata in Southeastern Nigeria. *Journal of African Earth Sciences*, 41, 79–
750 101. <https://doi.org/10.1016/j.jafrearsci.2005.02.002>

751 Pausas, J. G., & Bradstock, R. A. (2007). Fire persistence traits of plants along a productivity and
752 disturbance gradient in mediterranean shrublands of south-east Australia. *Global Ecology and*
753 *Biogeography*, 16(3), 330 – 340. <https://doi.org/10.1111/j.1466-8238.2006.00283.x>

754 Pausas, J. G., & Paula, S. (2012). Fuel shapes the fire–climate relationship: evidence from
755 Mediterranean ecosystems. *Global Ecology and Biogeography*, 21(11), 1074 – 1082.
756 <https://doi.org/10.1111/j.1466-8238.2012.00769.x>

757 Pausas, J. G., & Ribeiro, E. (2013). The global fire–productivity relationship. *Global Ecology and*
758 *Biogeography*, 22(6), 728 – 736. <https://doi.org/10.1111/geb.12043>

759 Petschick, R. MacDiff 4.1. 2. Powder diffraction software (2000). Available from the author at
760 <http://www.geol.uni-erlangen.de/html/software/Macdiff.html>.

761 Pieńkowski, G., Uchman, A., Ninard, K., & Hesselbo, S. P. (2021). Ichnology, sedimentology, and
762 orbital cycles in the hemipelagic Early Jurassic Laurasian Seaway (Pliensbachian, Cardigan Bay
763 Basin, UK). *Global and Planetary Change*, 207, 103648.
764 <https://doi.org/10.1016/j.gloplacha.2021.103648>

765 Rees, P. M., Ziegler, A. M. & Valdes, P. J. (2000). Jurassic phytogeography and climates: new data
766 and model comparisons. In Huber, B. T., Macleod, K. G. & Wing, S. L. (Eds.), *Warm Climates in*
767 *Earth History*. (pp. 297 – 318). Cambridge: Cambridge University Press.

768 Retallack, G. J. (2001). A 300-million-year record of atmospheric carbon dioxide from fossil plant
769 cuticles. *Nature*, 411(6835), 287 – 290. <https://doi.org/10.1038/35077041>

770 Riding, J. B., Leng, M. J., Kender, S., Hesselbo, S. P., & Feist-Burkhardt, S. (2013). Isotopic and
771 palynological evidence for a new Early Jurassic environmental perturbation. *Palaeogeography,*
772 *Palaeoclimatology, Palaeoecology*, 374, 16 – 27. <https://doi.org/10.1016/j.palaeo.2012.10.019>

773 Robinson, S. A., Ruhl, M., Astley, D. L., Naafs, B. D. A., Farnsworth, A. J., Bown, P. R. et al. (2017).
774 Early Jurassic North Atlantic sea-surface temperatures from TEX⁸⁶ palaeothermometry.
775 *Sedimentology*, 64(1), 215 – 230. <https://doi.org/10.1111/sed.12321>

776 Rubincam, D. P. (1994). Insolation in terms of Earth's orbital parameters. *Theoretical and applied*
777 *climatology*, 48, 195 – 202. <https://doi.org/10.1007/BF00867049>

778 Ruffell, A., McKinley, J. M. & Worden, R. H. (2002). Comparison of clay mineral stratigraphy to
779 other proxy palaeoclimate indicators in the Mesozoic of NW Europe. *Philosophical Transactions of*
780 *the Royal Society London A: Mathematical, Physical and Engineering Sciences*, 360, 675 – 693.
781 <https://doi.org/10.1098/rsta.2001.0961>

782 Ruhl, M., Hesselbo, S. P., Hinnov, L., Jenkyns, H. C., Xu, W., Riding, J. B., et al. (2016).
783 Astronomical constraints on the duration of the Early Jurassic Pliensbachian Stage and global climatic
784 fluctuations. *Earth and Planetary Science Letters*, 455, 149 – 165.
785 <https://doi.org/10.1016/j.epsl.2016.08.038>

786 Scott, A. C. (2000). The Pre-Quaternary history of fire. *Palaeogeography, Palaeoclimatology,*
787 *Palaeoecology*, 164(1-4), 281 – 329. [https://doi.org/10.1016/S0031-0182\(00\)00192-9](https://doi.org/10.1016/S0031-0182(00)00192-9)

788 Scott, A. C., & Damblon, F. (2010). Charcoal: Taphonomy and significance in geology, botany and
789 archaeology. *Palaeogeography, Palaeoclimatology, Palaeoecology*, 291(1-2), 1 – 10.
790 <https://doi.org/10.1016/j.palaeo.2010.03.044>

791 Sellwood, B. W., & Valdes, P. J. (2008). Jurassic climates. *Proceedings of the Geologists'*
792 *Association*, 119(1), 5 – 17. [https://doi.org/10.1016/S0016-7878\(59\)80068-7](https://doi.org/10.1016/S0016-7878(59)80068-7)

793 Silva, R. L., Duarte, L. V., Wach, G. D., Ruhl, M., Sadki, D., Gómez, J. J. et al. (2021). An Early
794 Jurassic (Sinemurian–Toarcian) stratigraphic framework for the occurrence of organic matter
795 preservation intervals (OMPIs). *Earth-Science Reviews*, 221, 103780.

796 Slater, S. M., Twitchett, R. J., Danise, S., & Vajda, V. (2019). Substantial vegetation response to Early
797 Jurassic global warming with impacts on oceanic anoxia. *Nature Geoscience*, 12(6), 462 – 467.
798 <https://doi.org/10.1038/s41561-019-0349-z>

799 Steinhorsdottir, M., & Vajda, V. (2015). Early Jurassic (late Pliensbachian) CO₂ concentrations
800 based on stomatal analysis of fossil conifer leaves from eastern Australia. *Gondwana Research*, 27(3),
801 932 – 939. <https://doi.org/10.1016/j.gr.2013.08.021>

802 Storm, M. S., Hesselbo, S. P., Jenkyns, H. C., Ruhl, M., Ullmann, C. V., Xu, W., et al. (2020). Orbital
803 pacing and secular evolution of the Early Jurassic carbon cycle. *Proceedings of the National Academy*
804 *of Sciences*, 117(8), 3974 – 3982. <https://doi.org/10.1073/pnas.1912094117>

805 The MathWorks Inc. (2021). MATLAB version: 9.11.0 (R2021b), Natick, Massachusetts: The
806 MathWorks Inc. <https://www.mathworks.com>

807 The MathWorks Inc. (2023). MATLAB version: 9.14.0 (R2023b), Natick, Massachusetts: The
808 MathWorks Inc. <https://www.mathworks.com>

809 Torsvik, T. H., & Cocks, L. R. M. (2017). Jurassic. In *Earth History and Palaeogeography*.
810 Cambridge: Cambridge University Press.

811 Trenberth, K. E., Fasullo, J., & Smith, L. (2005). Trends and variability in column-integrated
812 atmospheric water vapor. *Climate dynamics*, 24(7), 741 – 758. [https://doi.org/10.1007/s00382-005-](https://doi.org/10.1007/s00382-005-0017-4)
813 [0017-4](https://doi.org/10.1007/s00382-005-0017-4)

814 Ullmann, C. V., Szücs, D., Jiang, M., Hudson, A. J., & Hesselbo, S. P. (2022). Geochemistry of
815 microfossil, bulk rock and secondary calcite in the Early Jurassic strata of the Llanbedr (Mochras
816 Farm) drill core, Cardigan Bay Basin, Wales, UK. *Journal of the Geological Society*, 179(1).
817 <https://doi.org/10.1144/jgs2021-018>

818 van de Schootbrugge, B., Bailey, T. R., Rosenthal, Y., Katz, M. E., Wright, J. D., Miller, K. G., et al.
819 (2005). Early Jurassic climate change and the radiation of organic-walled phytoplankton in the Tethys
820 Ocean. *Paleobiology*, 31(1), 73 – 97. [https://doi.org/10.1666/0094-](https://doi.org/10.1666/0094-8373(2005)031<0073:EJCCAT>2.0.CO;2)
821 [8373\(2005\)031<0073:EJCCAT>2.0.CO;2](https://doi.org/10.1666/0094-8373(2005)031<0073:EJCCAT>2.0.CO;2)

822 van der Werf, G. R., Randerson, J. T., Giglio, L., Collatz, G. J., Kasibhatla, P. S., & Arellano Jr, A. F.
823 (2006). Interannual variability in global biomass burning emissions from 1997 to 2004. *Atmospheric*
824 *Chemistry and Physics*, 6(11), 3423 – 3441. <https://doi.org/10.5194/acp-6-3423-2006>

825 Van Konijnenburg-Van Cibert, J. H. A. (2002). Ecology of some late Triassic to early Cretaceous
826 ferns in Eurasia. *Review of Palaeobotany and Palynology*, 119(1-2), 113 – 124.
827 [https://doi.org/10.1016/S0034-6667\(01\)00132-4](https://doi.org/10.1016/S0034-6667(01)00132-4)

828 Westerhold, T., Marwan, N., Drury, A. J., Liebrand, D., Agnini, C., Anagnostou, E. et al. (2020). An
829 astronomically dated record of Earth’s climate and its predictability over the last 66 million years.
830 *Science*, 369(6509), 1383 – 1387. <https://doi.org/10.1126/science.aba6853>

831 Willes, K. & McElwain, J. (2014) *The Evolution of Plants*, Oxford University Press.